A High-Efficiency Charger With Adaptive Input Ripple MPPT for Low-Power Thermoelectric Energy Harvesting Achieving 21% Efficiency Improvement

Junwon Jeong, *Student Member, IEEE*, Minseob Shim, *Member, IEEE*, Junyoung Maeng, *Student Member, IEEE*, Inho Park, *Student Member, IEEE*, and Chulwoo Kim, *Senior Member, IEEE*

***Abstract*—A high-efficiency charger for low-power thermoelectric energy harvesting with a method for improving the efficiency, which is called the adaptive input ripple (AIR) maximum power point tracking (MPPT) technique, is introduced in this paper. On the basis of the key finding that the end-to-end efficiency ($\eta_{E\text{-}E}$) is highly dependent on the amplitude of the input ripple of the charger ($\Delta V_{\rm IN}$) in the low-power region, the proposed AIR MPPT technique adjusts $\Delta V_{\rm IN}$ to maximize $\eta_{E\text{-}E}$. Moreover, the minimum input power that allows the charger to maintain operation is enhanced by the proposed AIR MPPT technique. The proposed charger is implemented with 180-nm complementary metal oxide–semiconductor technology. An improvement of 21% in $\eta_{E\text{-}E}$ is achieved with the proposed technique. Furthermore, the proposed technique enhances the minimum power by 7.5 μW. The startup power and minimum power of the prototype are 37 and 6 μW, respectively. The maximum $\eta_{E\text{-}E}$ is 82%.**

***Index Terms*—Adaptive input ripple (AIR), charger, energy harvesting, low power, maximum power point tracking (MPPT), thermoelectric generator (TEG).**

I. Introduction

ADVANCES in the complementary metal oxide–semiconductor (CMOS) processes and low-power design techniques keep decreasing the power consumption of Internet of Things (IoT) devices [1]–[4]. Therefore, harvesting even a small amount of energy can provide a substitute for the batteries in such devices whose battery replacement is difficult. Using energy harvesting, the operating lifetime of IoT devices can be prolonged without replacing the battery. For example, [4] introduces a wireless sensor node system supplied by energy harvesting with an input power of 4 μW. Energy harvesters convert the environmental energy (solar, vibrational, thermal, frictional, radio frequency (RF), or bioenergy) into the electrical energy.

Manuscript received November 14, 2018; revised February 19, 2019; accepted April 4, 2019. Date of publication April 17, 2019; date of current version October 18, 2019. This work was supported by the National Research Foundation of Korea (NRF) grant funded by the Korea government (MSIT) 2016RIEIAIA02922127. Recommended for publication by Associate Editor C. Fernandez *(Corresponding author: Chulwoo Kim.)*

The authors are with the Department of Electrical Engineering, Korea University, Seoul 02841, South Korea (e-mail: jjw@kilby.korea.ac.kr; sms@kilby.korea.ac.kr; mjy@kilby.korea.ac.kr; pih@kilby.korea.ac.kr; ckim@kilby.korea.ac.kr).

Color versions of one or more of the figures in this paper are available online at http://ieeexplore.ieee.org.

Digital Object Identifier 10.1109/TPEL.2019.2912030

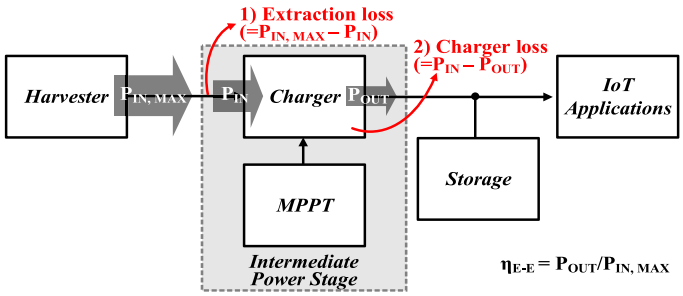

Fig. 1. Block diagram of IoT devices with energy harvesting.

Even though the power dissipation of the building blocks in IoT devices has been decreased as described previously, this power reduction has not been directly reflected in the advances in the operating lifetime of devices that are supplied with the battery [5]. That is because the portion of the power losses from the intermediate power stage is large especially in the low-power region. Fig. 1 shows a block diagram of IoT devices with energy harvesting, which consists of an energy harvester, storage, IoT applications, and the intermediate power stage. The intermediate power stage is composed of a charger and maximum power point tracking (MPPT) block. The charger up/downconverts the harvester output into an appropriate supply voltage level for the IoT applications. The MPPT block allows the charger to extract the maximum power from the harvester by regulating the input of the charger at the maximum power point (MPP). Even though the harvested power level is scaled down, the power losses in the intermediate power stage cannot be decreased at a similar proportion. Therefore, the end-to-end power conversion efficiency η_{E-E}, which is the ratio between the output power of the intermediate power stage ($P_{\rm OUT}$) and the maximum power that can be extracted from the harvester ($P_{\rm IN,\ MAX}$), becomes lower as the power level decreases.

The power losses in the intermediate power stage mainly consist of two parts: 1) extraction and 2) charger losses; both of them should be carefully considered to achieve the maximum η_{E-E}. The extraction loss is the power that is lost at the harvester/intermediate power stage interface because the input of the intermediate stage is not regulated at the MPP accurately and can be expressed as $P_{\rm IN,\ MAX} - P_{\rm IN}$, where $P_{\rm IN}$ is the effective input power of the intermediate power stage. The charger

loss is composed of the switching and conduction losses of the charger and is equal to $P_{\rm OUT} - P_{\rm IN}$. To maximize η_{E-E}, appropriate values of both extraction and charger losses are required. Many conventional approaches have been introduced to reduce the extraction and charger losses [5], [9]–[26]. To decrease the extraction loss, these techniques mainly focus on regulating the average value of input charger at a fraction of harvester open-circuit voltage for MPPT. However, the extraction loss resulting from the input ripple of the charger is not considered properly in the conventional works. The amount of the input ripple, as well as the average input regulation, should be taken into account at the low-power region. Switching frequency of the charger can be reduced to decrease the charger loss at the low-power region because the switching loss holds a dominant portion of the total charger loss. Reducing the switching frequency increases the input ripple of the charger considering that large input capacitor is undesirable to maintain a small form factor of IoT devices. In this case, extraction loss can increase even though the average input of the charger is regulated at MPP. Therefore, η_{E-E} can be limited due to the extraction loss coming from the input ripple. This relationship is discussed in detail in Section III.

Energy harvesting with thermoelectric generators (TEGs) is one of the best solutions for supplying power to body-worn and industrial sensors [6]–[8]. Several charger techniques for thermoelectric energy harvesting for enhancing the power-conversion efficiency and achieving self-startup have been introduced [5], [9]–[26]. However, the most conventional approaches provide low efficiencies at low-power levels. Efficient control schemes [9]–[12] have been reported to increase the efficiency. In addition, self-startup techniques have been proposed to enable self-startup [13]–[17]. However, they [9]–[17] lack MPPT control, which is essential to harvest the maximum power from varying ambient sources. Several MPPT methods have been introduced [18]–[21]. However, precharged storage is required for startup [18]–[20], and no self-startup techniques have been addressed [21]. Furthermore, one more charger output is required to achieve a high efficiency [19], [20]. Several MPPT techniques with various self-startup schemes have been reported [5], [22]–[26]. However, the extraction loss due to input ripple is not dealt with in [5], [9]–[26], and their efficiencies at a low power remain poor (53% at an input power of 24 μW [26]).

In this paper, a technique for maximizing η_{E-E} in the low-power region, which is called an adaptive input ripple (AIR) MPPT method, is proposed. The AIR MPPT technique takes into account both extraction and charger losses and controls the input ripple of the charger $\Delta V_{\rm IN}$ according to the input power level. Therefore, improvements in η_{E-E} and minimum power can be achieved. Furthermore, fully electrical self-startup in the low-power region can be provided.

Section II describes the relationships among η_{E-E}, extraction, and charger losses. On the basis of the description in Section II, the relationship between the switching frequency and the input ripple is analyzed in Section III; then, the relationships between the input ripple and the efficiencies are discussed. On the basis of these relationships, the AIR MPPT technique is proposed. Section IV highlights the issues pertaining to the circuit implementation of the proposed charger with the AIR MPPT method. Section V presents the measurement results for a prototype chip. Finally, the conclusions are presented in Section VI.

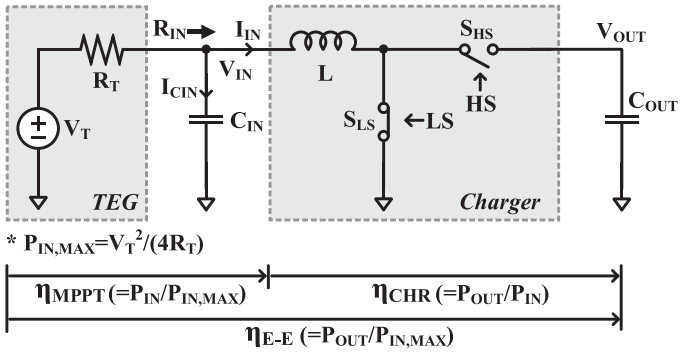

Fig. 2. Structure of the thermal energy harvesting system.

II. End-to-End, Charger, and MPPT Efficiencies

Fig. 2 shows the basic structure of a thermal energy harvesting system, which consists of a TEG, a charger, and input/output capacitors $C_{\rm IN}$/$C_{\rm OUT}$. The TEG is modeled as a voltage source V_T with an internal resistance R_T. V_T is an open-circuit voltage of the TEG, which is proportional to the Seebeck coefficient and the temperature difference between both sides of the TEG. The charger is composed of an inductor L, a high-side switch $S_{\rm HS}$, and a low-side switch $S_{\rm LS}$ and converts the low-voltage input $V_{\rm IN}$ to the output voltage $V_{\rm OUT}$, which is sufficiently high for the load circuits. $S_{\rm HS}$ and $S_{\rm LS}$ are controlled by the gate signals *HS* and *LS*, respectively, to achieve MPPT and power delivery to the output capacitor $C_{\rm OUT}$. To deliver the maximum power from the TEG to the output of the charger, η_{E-E} should be preferentially considered, which can be expressed as

$$\eta_{E-E} = \frac{P_{\rm OUT}}{P_{\rm IN,MAX}} \tag{1}$$

where $P_{\rm IN,\ MAX}$ is the maximum power that the charger can extract from the TEG. According to the maximum power transfer theory, $P_{\rm IN,\ MAX}$ is achieved when the load resistance of the TEG, which is the same with the effective input resistance of the charger ($R_{\rm IN}$), is equal to R_T. Therefore, V_T is divided by half at $V_{\rm IN}$, and $P_{\rm IN,\ MAX}$ can be expressed as

$$P_{\rm IN,MAX} = \frac{V_T^2}{4R_T}. \tag{2}$$

When $R_{\rm IN}$ is matched with R_T, it can be said that the charger operates at the MPP. The two main power losses that degrade η_{E-E} are the extraction and charger losses. The extraction loss is defined as the power loss originating from the impedance mismatch between R_T and $R_{\rm IN}$. The relative power delivered to the input of the charger over $P_{\rm IN,\ MAX}$ regarding the extraction loss can be represented by the MPPT efficiency $\eta_{\rm MPPT}$, which is

$$\eta_{\rm MPPT} = \frac{P_{\rm IN,AVR}}{P_{\rm IN,MAX}} \tag{3}$$

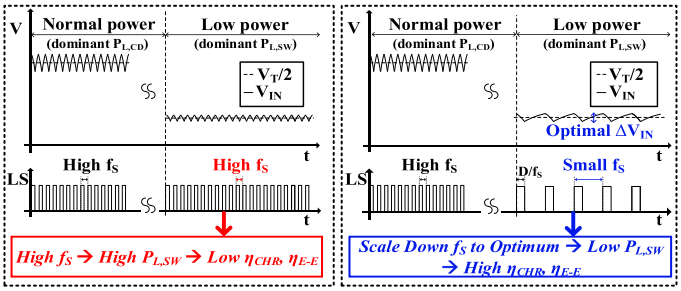

Fig. 3. Comparison between the (a) conventional and (b) proposed AIR MPPT techniques.

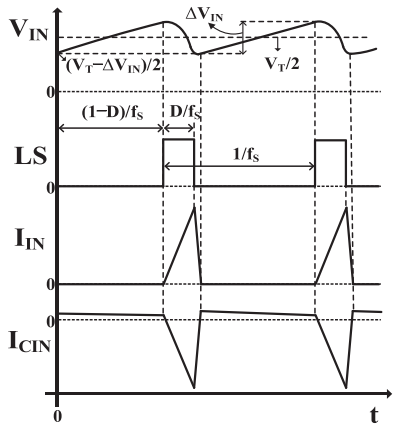

Fig. 4. Timing diagram of the charger in the steady state.

where $P_{\mathrm{IN,AVR}}$ is the average input power to the charger. The charger loss is defined as the power loss at the charger and mainly originates from the conduction and switching losses of the charger. Accounting for the charger loss, the power delivered to the output of the charger over $P_{\mathrm{IN,AVR}}$ can be represented by the charger efficiency η_{CHR}, which is

$$\eta_{\mathrm{CHR}} = \frac{P_{\mathrm{OUT}}}{P_{\mathrm{IN,AVR}}}. \tag{4}$$

Therefore, η_{E-E} is

$$\eta_{E-E} = \eta_{\mathrm{MPPT}} \cdot \eta_{\mathrm{CHR}}. \tag{5}$$

To maximize η_{E-E}, both η_{MPPT} and η_{CHR} should be carefully adjusted to their optimum values.

III. Proposed AIR MPPT

Fig. 3 shows a comparison between the conventional MPPT and proposed AIR MPPT techniques. When *LS* is "high," S_{LS} is turned ON, and the inductor current I_{IN} is built up, yielding a negative net current flowing to C_{IN}. Therefore, V_{IN} is decreased. If *LS* is "low," S_{LS} is turned OFF, and S_{HS} is turned ON. Therefore, I_{IN} decreases, yielding a positive net current to C_{IN} and an increase in V_{IN}. Repeating these procedures, V_{IN} is regulated at half of V_T, which is the MPP. In the low-power region, η_{CHR} is highly dominated by the switching loss ($P_{L,\mathrm{SW}}$) rather than the conduction loss ($P_{L,\mathrm{CD}}$) of the charger. However, the conventional MPPT cannot control the switching frequency of *LS* (f_S) according to the level of P_{IN}. Therefore, a high f_S in the low-power region of the conventional MPPT techniques leads to a high $P_{L,\mathrm{SW}}$, which significantly degrades η_{CHR}. The proposed AIR MPPT technique dynamically adjusts f_S according to the level of P_{IN}. In the normal input power region, a high f_S is selected because η_{CHR} and η_{E-E} are dominated by $P_{L,\mathrm{CD}}$ rather than $P_{L,\mathrm{SW}}$. In the low-input-power region, f_S is scaled down to optimal value, and $P_{L,\mathrm{SW}}$ is reduced. Therefore, η_{CHR} and η_{E-E} are enhanced because they are highly dependent on $P_{L,\mathrm{SW}}$.

f_S cannot be decreased infinitely and has an optimal value to maximize η_{E-E} because a smaller f_S leads to a lower η_{MPPT} with a fixed C_{IN}. A small C_{IN} is desired for a small form factor. The smaller f_S causes a large input ripple ΔV_{IN}, which degrades η_{MPPT}. This degradation in η_{MPPT} is especially critical for thermoelectric energy harvesting because the output voltage of the harvester is smaller compared with other energy harvesting applications such as solar and piezoelectric. Fig. 4 shows the timing diagram of the charger in the steady state. The charger operates in the discontinuous conduction mode (DCM), and I_{IN} is zero, while both S_{LS} and S_{HS} are turned OFF in the steady state. Therefore, only the charge from the TEG is accumulated in C_{IN}. When both S_{LS} and S_{HS} are turned OFF, V_{IN} as a function of the time t can be expressed as

$$V_{\mathrm{IN}}(t) = \frac{1}{2}(V_T - \Delta V_{\mathrm{IN}}) + \frac{1}{C_{\mathrm{IN}}}\int_0^t \frac{V_T - V_{\mathrm{IN}}(x)}{R_T}dx. \tag{6}$$

Taking the Laplace transform of both sides of (6),

$$\mathcal{L}\{V_{\mathrm{IN}}(t)\} = \frac{\frac{V_T-\Delta V_{\mathrm{IN}}}{2}s + \frac{V_T}{C_{\mathrm{IN}}R_T}}{s^2 + \frac{1}{C_{\mathrm{IN}}R_T}s}. \tag{7}$$

Taking inverse Laplace transform of both sides of (7),

$$V_{\mathrm{IN}}(t) = V_T - \frac{V_T + \Delta V_{\mathrm{IN}}}{2}e^{-\frac{t}{C_{\mathrm{IN}}R_T}}. \tag{8}$$

Therefore, ΔV_{IN} can be expressed as

$$\Delta V_{\mathrm{IN}} = V_{\mathrm{IN}}(t)|_{t=(1-D)/f_S} - V_{\mathrm{IN}}(t)|_{t=0} = \frac{V_T+\Delta V_{\mathrm{IN}}}{2}\left(1-e^{-\frac{1-D}{C_{\mathrm{IN}}R_T f_S}}\right) \tag{9}$$

where D is the duty cycle of *LS*. Solving (9), ΔV_{IN} is

$$\Delta V_{\mathrm{IN}} = V_T\left(\frac{1-e^{-\frac{1-D}{C_{\mathrm{IN}}R_T f_S}}}{1+e^{-\frac{1-D}{C_{\mathrm{IN}}R_T f_S}}}\right). \tag{10}$$

If the system operates at the MPP, R_T and R_{IN} should be matched and can be expressed as [5]

$$R_T = R_{\mathrm{IN}} = \frac{2Lf_S}{D^2}. \tag{11}$$

Combining (10) and (11), ΔV_{IN} can be expressed as

$$\Delta V_{\mathrm{IN}} = V_T\left(\frac{1-e^{-\frac{1-\sqrt{2Lf_S/R_T}}{C_{\mathrm{IN}}R_T f_S}}}{1+e^{-\frac{1-\sqrt{2Lf_S/R_T}}{C_{\mathrm{IN}}R_T f_S}}}\right). \tag{12}$$

According to (12), a smaller f_S yields a larger $\Delta V_{\rm IN}$ for a fixed $C_{\rm IN}$. $P_{\rm IN,AVR}$ is

$$P_{\rm IN,AVR} = f_S \int_{(1-D)/f_S}^{(1-D)/f_S+D/f_S} P_{\rm IN}(t)\,dt = f_S \int_{(1-D)/f_S}^{(1-D)/f_S+D/f_S} V_{\rm IN}(t)\cdot I_{\rm IN}(t)\,dt. \quad (13)$$

It can be assumed that the on time of $S_{\rm HS}$ is negligibly small compared with that of $S_{\rm LS}$ and that $V_{\rm IN}(t)$ is linear in t for a simpler derivation, while LS is "low" because $C_{\rm IN}$ is considerably larger. Therefore, $V_{\rm IN}(t)$ and $I_{\rm IN}(t)$ are

$$V_{\rm IN}(t) = \frac{V_T + \Delta V_{\rm IN}}{2} - \frac{\Delta V_{\rm IN}}{D/f_S}\left[t - (1-D)/f_S\right], \quad (14)$$

$$I_{\rm IN}(t) = \frac{V_{\rm IN}(t)}{L}\left[t - (1-D)/f_S\right]. \quad (15)$$

Combining (11), (13), (14), and (15), $P_{\rm IN,AVR}$ is expressed as

$$P_{\rm IN,AVR} = \frac{f_S}{L}\int_{(1-D)/f_S}^{(1-D)/f_S+D/f_S} V_{\rm IN}^2(t)\cdot t dt = \frac{2V_T^2 + (V_T - \Delta V_{\rm IN})^2}{12R_T}. \quad (16)$$

Therefore, if $\Delta V_{\rm IN}$ is smaller than V_T, a larger $\Delta V_{\rm IN}$ decreases $P_{\rm IN,AVR}$ and $\eta_{\rm MPPT}$, which is

$$\eta_{\rm MPPT} = \frac{P_{\rm IN,AVR}}{P_{\rm IN,MAX}} = \frac{2V_T^2 + (V_T - \Delta V_{\rm IN})^2/12R_T}{V_T^2/4R_T} = \frac{2V_T^2 + (V_T - \Delta V_{\rm IN})^2}{3V_T^2}. \quad (17)$$

On the basis of (12) and (17), a smaller f_S for a higher $\eta_{\rm CHR}$ yields a larger $\Delta V_{\rm IN}$, which degrades $\eta_{\rm MPPT}$. Therefore, $\Delta V_{\rm IN}$, which is directly related to f_S, should be regulated at the optimal value to maximize η_{E-E}. The f_S scaling technique was introduced in [20]; however, it only takes into account the charger loss ($\eta_{\rm CHR}$) and does not consider the extraction loss ($\eta_{\rm MPPT}$), which can degrade η_{E-E} when f_S is scaled down further with fixed $C_{\rm IN}$.

Fig. 5 shows the simulation results for η_{E-E}, $\eta_{\rm MPPT}$, and $\eta_{\rm CHR}$ as a function of $\Delta V_{\rm IN}$ at the normal input power ($P_{\rm IN,\,MAX}$ = 150 μW). The temperature difference between both sides of the TEG (ΔT) of 2.1 °C and 0% R_T variations are assumed. The charger used in the simulation consists of $C_{\rm IN}$ = 100 nF and L = 22 μH. The TEG is modeled by a series-connected R_T (= 1.68 kΩ) and voltage source V_T. The input power is changed by adjusting V_T. f_S is modulated to change $\Delta V_{\rm IN}$. D is also adjusted according to f_S for MPPT based on (10). The charger is assumed to eliminate all of the negative inductor current from $V_{\rm OUT}$ to V_X. As f_S decreases, $P_{L,\rm SW}$ is reduced, and $\eta_{\rm CHR}$ increases until $P_{L,\,\rm CD}$ dominates owing to the increased peak value of $I_{\rm IN}$. At the same time, $\eta_{\rm MPPT}$ decreases owing to the lower f_S, which yields a larger $\Delta V_{\rm IN}$ on the basis of (12) and (17). Therefore, η_{E-E} has the maximum value, where the product of $\eta_{\rm CHR}$ and $\eta_{\rm MPPT}$ becomes the highest on the basis of (5). With $P_{\rm IN,\,MAX}$ = 150 μW, the optimum $\Delta V_{\rm IN}$ and f_S for the maximum η_{E-E} are 56 mV and 60 kHz, respectively.

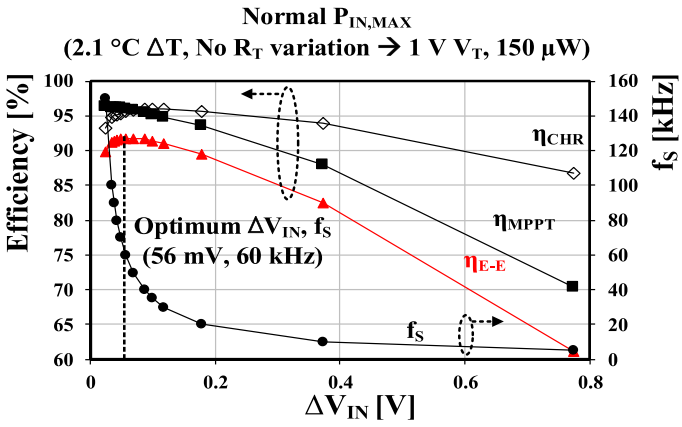

Fig. 5. Simulation results for $\eta_{\rm MPPT}$, $\eta_{\rm CHR}$, and η_{E-E} as a function of $\Delta V_{\rm IN}$ at the normal input power (150 μW) with no R_T variations.

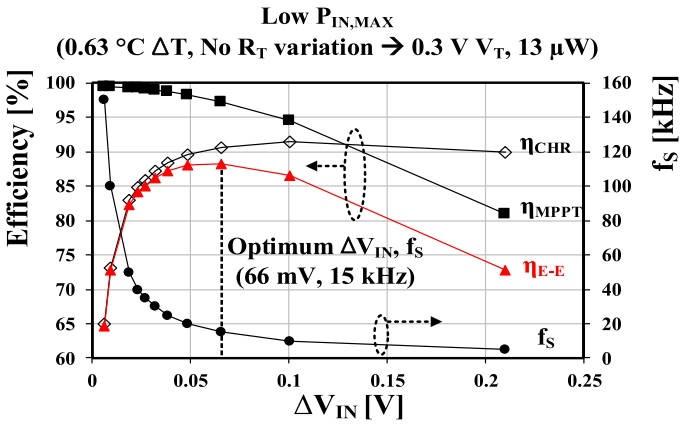

Fig. 6. Simulation results for $\eta_{\rm MPPT}$, $\eta_{\rm CHR}$, and η_{E-E} as a function of $\Delta V_{\rm IN}$ at a low input power (13 μW) with no R_T variations.

The optimum values of $\Delta V_{\rm IN}$ and f_S vary according to the input power level. Fig. 6 shows the simulation results of η_{E-E}, $\eta_{\rm MPPT}$, and $\eta_{\rm CHR}$ as a function of $\Delta V_{\rm IN}$ when a low input power ($P_{\rm IN,\,MAX}$ = 13 μW) is applied. ΔT of 0.63 °C and 0% R_T variations are assumed. The optimum $\Delta V_{\rm IN}$ and f_S are 66 mV and 15 kHz with this input power. The optimal f_S is smaller compared with the simulation results with $P_{\rm IN,\,MAX}$ = 150 μW because $P_{L,\rm SW}$ is more dominant in the low-power region compared with that in the normal-power region.

Fig. 7 shows the simulation results of η_{E-E}, $\eta_{\rm MPPT}$, and $\eta_{\rm CHR}$ with R_T variations. R_T of TEG depends on the temperature difference between two terminals of TEG. R_T can deviate by 12% from the design value [27]. Therefore, the optimum $\Delta V_{\rm IN}$ and f_S for the maximum η_{E-E} will change from the desired value according to the variations of R_T. To figure out the variations of $\Delta V_{\rm IN}$ and f_S according to R_T variations, same values of ΔT (2.1 °C for the normal $P_{\rm IN,\,MAX}$, 0.63 °C for the low $P_{\rm IN,\,MAX}$) are applied because the system controls $\Delta V_{\rm IN}$ and f_S based on the V_T information. R_T variations of + 12% give the optimum f_S variations of 10 kHz and 0 Hz for the normal

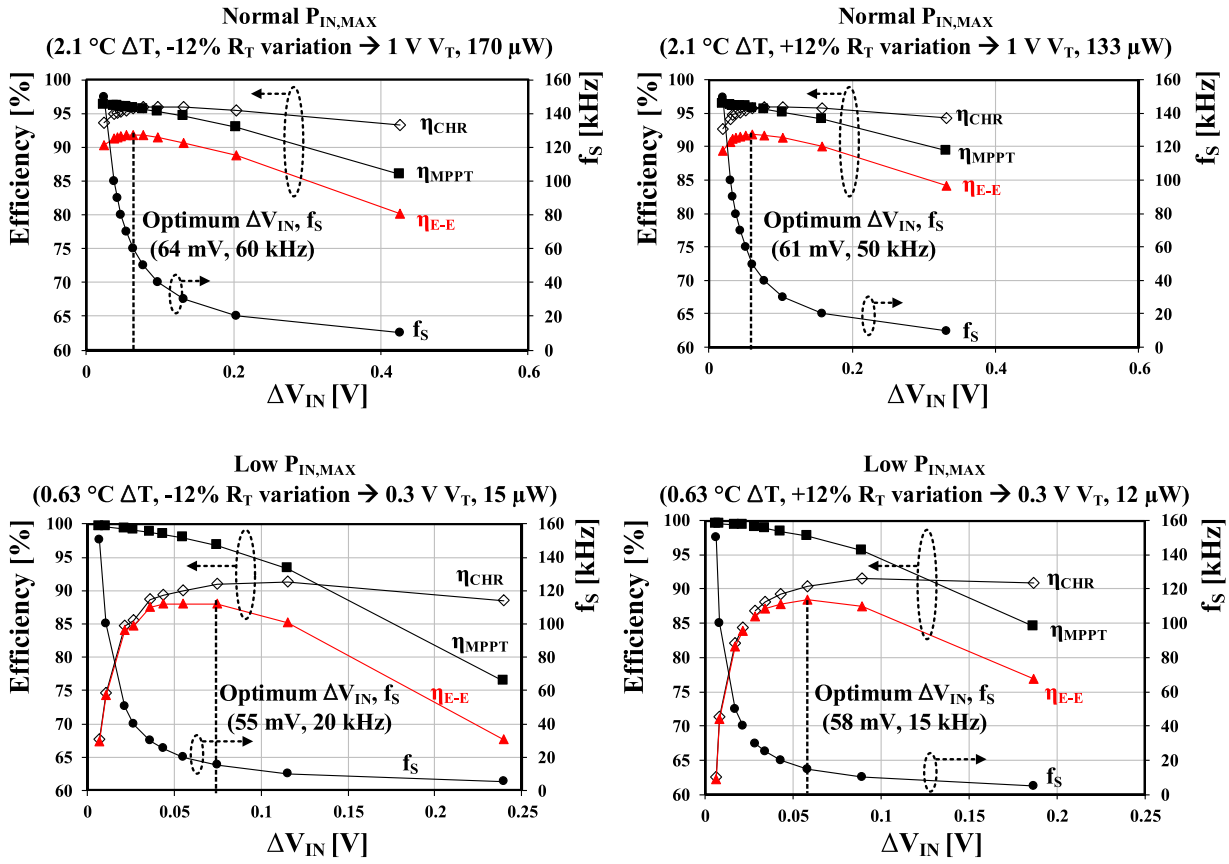

Fig. 7. Simulation results for η_{MPPT}, η_{CHR}, and η_{E-E} as a function of ΔV_{IN} at high/low input power with $\pm 12\%$ R_T variations.

and low input powers, respectively. However, η_{E-E} degradation due to 10 kHz f_S variation is not severe, which is 0.15% based on the simulation results. Variations of 0 Hz and 5 kHz on the optimum f_S result from –12% R_T variations. Variation of 5 kHz on the optimum f_S gives η_{E-E} degradation of 0.15%.

To improve η_{E-E}, the proposed AIR MPPT technique adjusts ΔV_{IN} by controlling f_S according to the input power level. For MPPT, V_{IN} is compared with half of V_T by a hysteresis comparator. To control ΔV_{IN} according to the input power level, a delay is added at the decision time of the hysteresis comparator. As the input power decreases, a larger delay is provided. Therefore, f_S decreases, and ΔV_{IN} becomes larger, achieving the maximum η_{E-E}. To verify the η_{E-E} improvements using the AIR MPPT technique, two levels of delay are implemented in this prototype. More delay levels can be added to improve η_{E-E} further across the whole input power range in future work.

IV. Circuit Implementation

A. Top Architecture

Fig. 8 shows the top architecture of the proposed energy harvesting system, which is composed of a charger, an AIR MPPT controller, a low-power starter (LPS), an S_{HS} controller, a capacitive divider, and a V_{DD} multiplexer (MUX). The AIR MPPT controller tracks the MPP and simultaneously controls ΔV_{IN} to improve η_{E-E}. The AIR MPPT controller provides V_N by comparing V_{IN} with $V_T/2$ generated by the capacitive divider. The

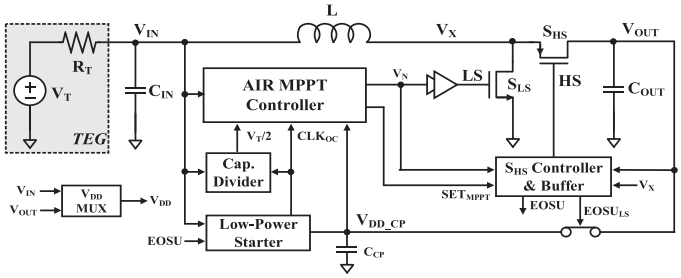

Fig. 8. Top architecture of the proposed energy harvesting system.

oscillator and frequency divider in the LPS provide the clock signal (CLK_{OC}) required for the capacitive divider to sense V_T. The LPS aids the self-startup of the charger even when a small temperature difference is applied to the TEG. Series-connected thin-film TEGs [28] are used to achieve fully electrical startup with the small temperature difference. The volume of the eight series-connected TEGs is ten times smaller than that of a single bulk TEG [29] that is used in the conventional architectures. The S_{HS} controller determines the ON-time of S_{HS} and maximizes the current flow from V_X to V_{OUT}. The buffer in the S_{HS} controller decreases the required minimum startup power by diode-connecting S_{HS} during startup. The S_{HS} controller also sets the end-of-startup signal (*EOSU*) "high" when V_{OUT} exceeds 0.7 V, which connects the output of the LPS ($V_{\mathrm{DD\_CP}}$) and V_{OUT}.

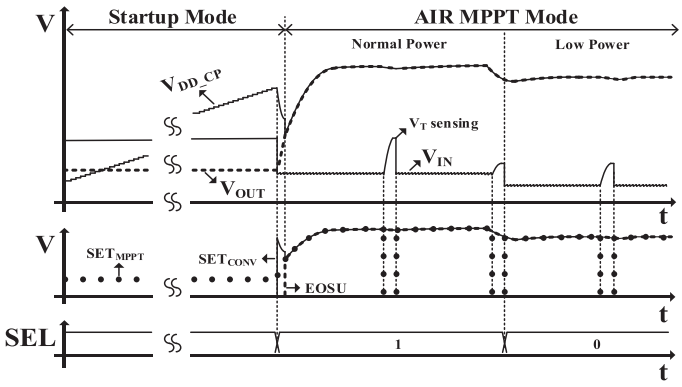

Fig. 9. Timing diagram of the proposed energy harvesting system.

Fig. 9 shows the timing diagram of the proposed energy harvesting system. The proposed system operates in two modes—the startup and AIR MPPT modes. During startup, $S_{\rm HS}$ is diode-connected, and no switching signal for $S_{\rm HS}$ is provided. Furthermore, the zero current switching (ZCS) block in the $S_{\rm HS}$ controller is disabled for further power saving. At the same time, the charge pump in the LPS provides charge stored in $C_{\rm CP}$ and generates $V_{\rm DD\_CP}$, which is the supply voltage of the AIR MPPT controller and control circuits. Once $V_{\rm DD\_CP}$ becomes larger than 1 V, $SET_{\rm CONV}$ becomes "high," and MPPT starts. $V_{\rm IN}$ is regulated at $V_T/2$, and harvested power is delivered to $V_{\rm OUT}$. When $V_{\rm OUT}$ becomes higher than 0.7 V, *EOSU* is set, and $V_{\rm DD\_CP}$ is connected to $V_{\rm OUT}$. From this point, $V_{\rm OUT}$ supplies the controllers, and startup is completed. In the AIR MPPT mode, both 1) MPPT and 2) η_{E-E} maximization can be achieved. For 1), the AIR MPPT controller compares $V_{\rm IN}$ with $V_T/2$ and generates *LS*. Then, the average $V_{\rm IN}$ is regulated at $V_T/2$, which is the MPP. For 2), the proposed switching time–controlled comparator (STC) in the AIR MPPT controller adjusts $\Delta V_{\rm IN}$, which is dependent on the power level, as discussed in Section III. The variable delay is given at the output of the STC, and the delay level is controlled by the selection signal *SEL*. For example, when a low-input power is applied, *SEL* becomes "0," and the maximum delay is chosen for the STC. This yields the smallest f_S, and consequently, $\Delta V_{\rm IN}$ becomes larger. When $V_{\rm IN}$ becomes higher than $V_T/2$, $S_{\rm LS}$ is turned ON, and $I_{\rm IN}$ is built up. $I_{\rm IN}$ decreases $V_{\rm IN}$, and when $V_{\rm IN}$ is lower than $V_T/2$, $S_{\rm LS}$ is turned OFF. Then, $S_{\rm HS}$ is turned ON, and $I_{\rm IN}$ flows to $V_{\rm OUT}$. The ON-time of $S_{\rm HS}$ is controlled by the ZCS block in the $S_{\rm HS}$ controller, which eliminates the reverse current from $V_{\rm OUT}$ to V_X.

B. AIR MPPT Controller

Fig. 10 shows a schematic of the proposed AIR MPPT controller, which consists of the STC, a low-power detector (LPD), a power-ON reset (PoR), and digital circuits. The STC compares $V_{\rm IN}$ and $V_T/2$ and turns ON $S_{\rm LS}$ when $V_{\rm IN}$ is larger than $V_T/2$. The low-power detector determines whether the input power is low or normal and sets *SEL* if the input power is above the threshold value (54 μW in this system). When *SEL* is "low," the STC decreases f_S and increases $\Delta V_{\rm IN}$.

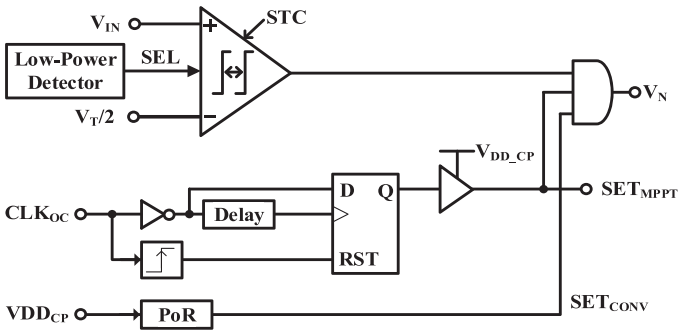

Fig. 10. Schematic of the proposed AIR MPPT controller.

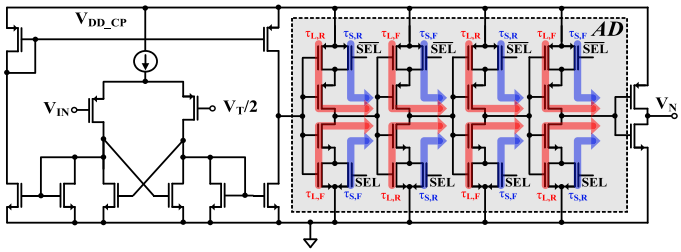

Fig. 11. Schematic of the proposed STC.

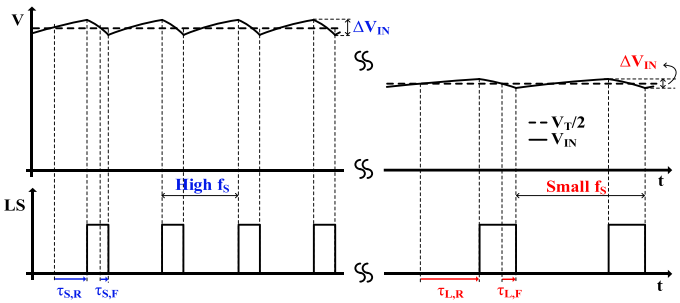

Fig. 12. Timing diagram of the STC.

Fig. 11 shows a schematic of the STC, which consists of a comparator and adaptive delay cells (*AD*). *AD* are composed of four series-connected delay cells, and each delay cell consists of large-length MOSFETs for the delay, bypass switches whose gates are controlled by *SEL*, and an inverter. Fig. 12 shows a timing diagram of the STC. If *SEL* is "low," the bypass switches are turned OFF, and long delays at the rising/falling edges of V_N ($\tau_{L,R}/\tau_{L,F}$) are added. The large-length MOSFETs have a two times smaller aspect ratio compared with the MOSFETs in the inverter. Four delay cells are series-connected to prevent the shoot-through current for power saving. Two delay levels are implemented in this design to verify the feasibility of the AIR MPPT. The number of the delay levels can be increased to further increase η_{E-E} across wide input power range.

C. Low-Power Starter

Fig. 13 shows a schematic of the LPS. The LPS consists of an oscillator, frequency dividers, a nonoverlapping clock generator, drivers, and an 18-stage charge pump. When the minimum $V_{\rm IN}$ required for generating the oscillator's clock is applied from the TEG, the oscillator starts to generate the clock signal $CLK_{\rm OSC}$.

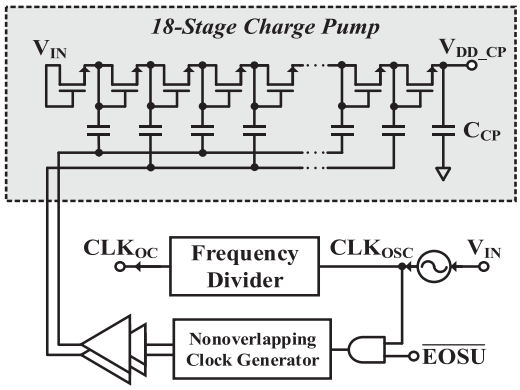

Fig. 13. Schematic of the LPS.

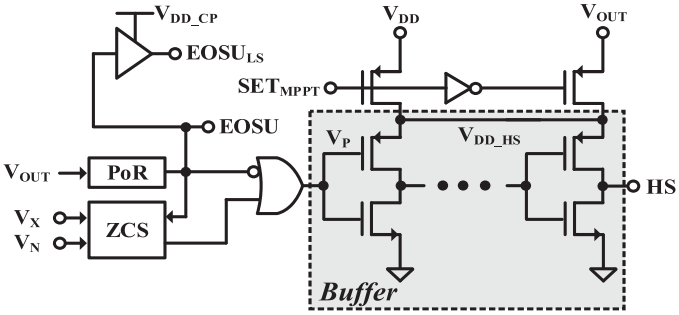

Fig. 14. Schematic of the $S_{\rm HS}$ controller and buffer.

The minimum $V_{\rm IN}$ for the oscillator is the startup voltage, which is 0.5 V. The output of the oscillator propagates to the nonoverlapping clock generator through an AND gate. The outputs of the nonoverlapping clock generator then propagate to the 18-stage charge pump. The 18-stage charge pump generates $V_{\rm DD\_CP}$, which is the internal supply of the system during startup by boosting $V_{\rm IN}$. After $V_{\rm OUT}$ becomes sufficiently high to complete startup, *EOSU* becomes "high," and the charge pump is turned OFF. Furthermore, the LPS also provides the clock signal $CLK_{\rm OC}$ required for the capacitive divider to sense V_T. The frequency of $CLK_{\rm OSC}$ is divided by a frequency divider, and $CLK_{\rm OC}$ is generated. $CLK_{\rm OSC}$ and $CLK_{\rm OC}$ are 51.2 kHz and 100 Hz, respectively.

D. $S_{\rm HS}$ Controller and Buffer

Fig. 14 shows a schematic of the $S_{\rm HS}$ controller and buffer. The ZCS block determines the ON-time of $S_{\rm HS}$ to deliver the maximum $I_{\rm IN}$ to $V_{\rm OUT}$. The PoR generates *EOSU*, which becomes "high" when $V_{\rm OUT}$ exceeds 0.7 V. In the startup mode, *EOSU* is "high," and V_P is also "high." Therefore, the buffer output *HS* is "high" with a value of $V_{\rm DD\_HS}$. $V_{\rm DD\_HS}$ is $V_{\rm DD}$ during the V_T-sensing period. Therefore, $S_{\rm HS}$ can be fully turned OFF during the V_T-sensing period in the startup mode, ensuring accurate V_T sensing.

Fig. 15 shows a schematic of the proposed ZCS block. The charger operates in the DCM rather than the continuous conduction mode to increase the power conversion efficiency for low-power applications [5], [10]. In the DCM, the turn-ON time of $S_{\rm HS}$ should be the optimal value to prevent the early or late

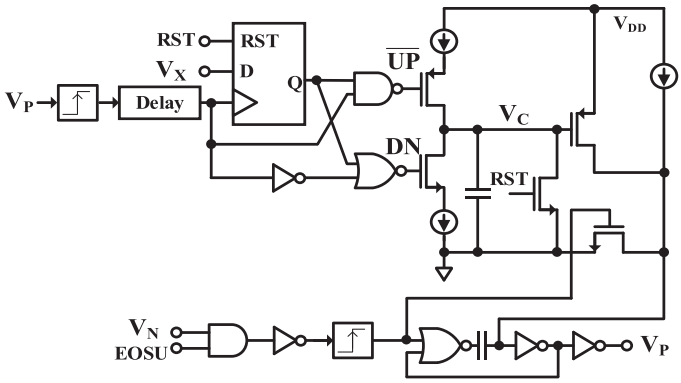

Fig. 15. Schematic of the ZCS block.

turn-OFF of $S_{\rm HS}$. When $S_{\rm HS}$ is turned OFF early, a positive $I_{\rm IN}$ still remains, and a body conduction loss is incurred at $S_{\rm HS}$. If $S_{\rm HS}$ is turned OFF late, a reverse $I_{\rm IN}$ leads to a degradation in the efficiency. Many conventional ZCS controls have been reported. The methods in [5], [10], [12], [13], [20], and [30] use the delay of the digital logic gates to adjust the ON-time of $S_{\rm HS}$. However, these methods suffer from a quantization error, which results in a large body conduction loss or a large reverse current in $S_{\rm HS}$. Furthermore, a large area and power consumption are required with these techniques when a longer ON-time of $S_{\rm HS}$ is desired. The methods in [23], [26], [31], and [32] use comparators, which have a comparator offset and a propagation delay due to the drivers. Therefore, the ZCS control with the comparators can be inaccurate, which decreases the efficiency. ZCS control with a wide range of ON-times for $S_{\rm HS}$ and a high resolution was introduced in [18]. However, it supplies an internal controller using an additional charged battery, which is not available for miniature IoT devices. If the system is fully self-powered, the ZCS controller in [18] cannot compare $V_{\rm OUT}$ with V_X, which becomes higher than $V_{\rm OUT}$ when $S_{\rm HS}$ is turned OFF early because the supply voltage of the ZCS controller cannot become higher than $V_{\rm OUT}$. ZCS control based on a simple one-shot pulse generator and D flip-flop is utilized in this system, enabling accurate ZCS control with a high accuracy and a wide range of $S_{\rm HS}$ ON-times, even when the system is self-powered. The proposed ZCS block consists of a one-shot pulse generator, edge detectors, and D flip-flops. V_P is generated from the one-shot pulse generator, which controls the pulsewidth with a charge pump. The output of the charge pump V_C is controlled by D flip-flops. If $S_{\rm HS}$ is turned OFF early, V_X is higher than $V_{\rm OUT}$, and logical "high" is sampled by the D flip-flops. The signal *UP* is generated, which increases V_C and extends the ON-time of $S_{\rm HS}$. If $S_{\rm HS}$ is turned OFF late, the D flip-flop samples logical "low" and generate the signal *DN*. Therefore, V_C becomes lower, which reduces the ON-time of $S_{\rm HS}$.

V. Measurement Results

Fig. 16 shows a prototype board for the post-silicon validation (left), and a microphotograph of the chip fabricated using 180-nm CMOS technology (right). The total active area of the chip is 1.1 mm^2. The input of the charger can be either real or

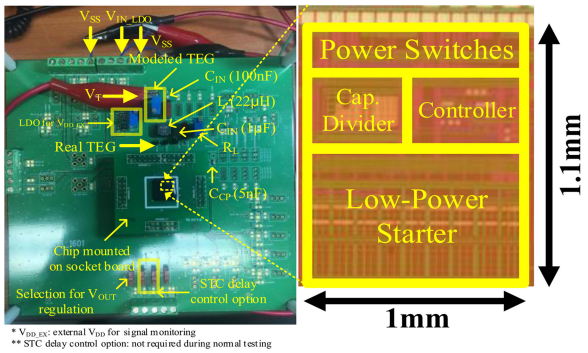

Fig. 16. Prototype board and microphotograph of a chip fabricated using 180-nm CMOS technology.

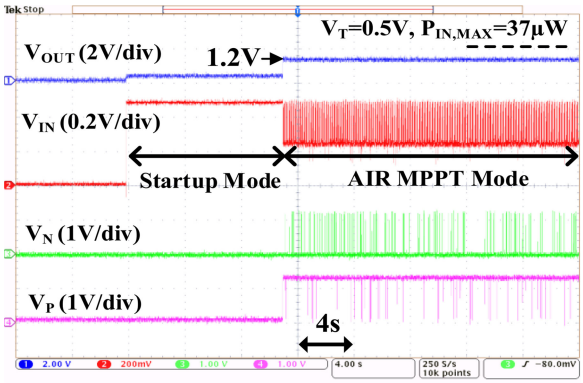

Fig. 17. Measured waveforms of the startup sequence of the proposed energy harvesting system.

modeled TEGs. The fabricated chip is mounted on the prototype board by socket board and pin headers. $V_{\rm OUT}$ can be optionally regulated at 1.2 V or not by controlling an external switch. Delay levels of the STC can be controlled externally only for the testing purposes (Fig. 21). In the normal operation of the prototype, no external controls are required. Nonsoldered parts of the prototype board are various testing options that were not used in the real testing. Fig. 17 shows the measured waveforms of the startup sequence of the proposed system. A 0.5-V voltage source in series with a 1.68-kΩ resistor emulate the TEGs with $P_{\rm IN,MAX} = 37\,\mu$W, $L = 22\,\mu$H, $C_{\rm IN} = 100$ nF, $C_{\rm OUT} = 1\,\mu$F, and $C_{\rm CP} = 5$ nF. During startup, no switching signals are generated for the power switches, and $V_{\rm IN}$ is nearly V_T. The oscillator in the LPS starts to provide a clock to the charge pump. The output of the charge pump ($V_{\rm DD\_CP}$) is not measured because probing the $V_{\rm DD\_CP}$ node can discharge $C_{\rm CP}$ owing to probe leakage. After the charge pump generates a sufficient $V_{\rm DD\_CP}$, MPPT begins, and V_N is generated to regulate $V_{\rm IN}$ at half of V_T (0.25 V). V_T is monitored periodically, and half of V_T is generated by the capacitive divider. The STC compares $V_{\rm IN}$ and divides V_T, and controls $S_{\rm LS}$. After *EOSU* is set, V_P controls $S_{\rm HS}$ to deliver the inductor current to the output. $V_{\rm OUT}$ is set to be 1.2 V by controlling the load conditions. Fig. 18 shows the measured waveforms of the proposed charger in the AIR MPPT mode. V_T (0.5 V) is periodically monitored, and $V_{\rm IN}$ is regulated at half of V_T (0.25 V). During V_T sensing phase, no switching signals

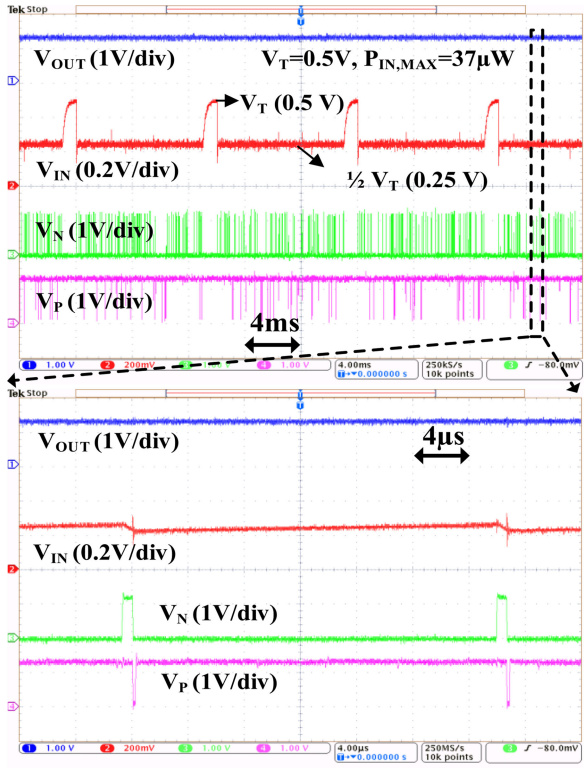

Fig. 18. Measured waveforms of the proposed energy harvesting system in the AIR MPPT mode.

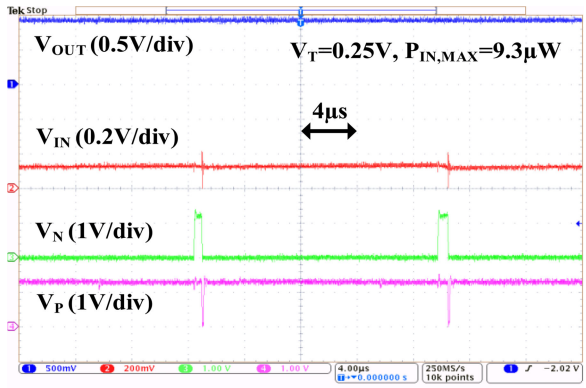

Fig. 19. Measured waveforms of the proposed energy harvesting system at $P_{\rm IN,MAX} = 9.3\,\mu$W.

for the power stage are generated to make input resistance of the charger large. When $V_{\rm IN}$ gets larger than 0.25 V, V_N becomes "high." $S_{\rm LS}$ is turned ON, and the inductor current is built up. $C_{\rm IN}$ is discharged by the inductor current, and $V_{\rm IN}$ decreases. Following a negative edge of V_N with a dead time, V_P becomes "low," and $S_{\rm HS}$ is turned ON, causing the inductor current to flow to $V_{\rm OUT}$. When the inductor current becomes zero, V_P becomes "high," and no current flows from $V_{\rm OUT}$. Fig. 19 shows the measured waveforms of the proposed charger at $P_{\rm IN,MAX} = 9.3\,\mu$W. $V_{\rm IN}$ is regulated at half of V_T (0.125 V) and is boosted at $V_{\rm OUT}$ at a small input power. A potentiometer is used to control the output load condition.

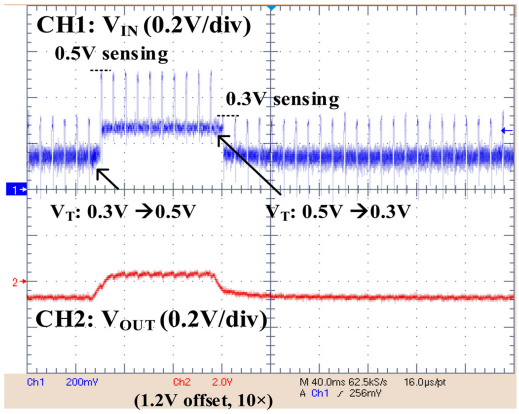

Fig. 20. Measured waveforms of the proposed energy harvesting system with V_T transient.

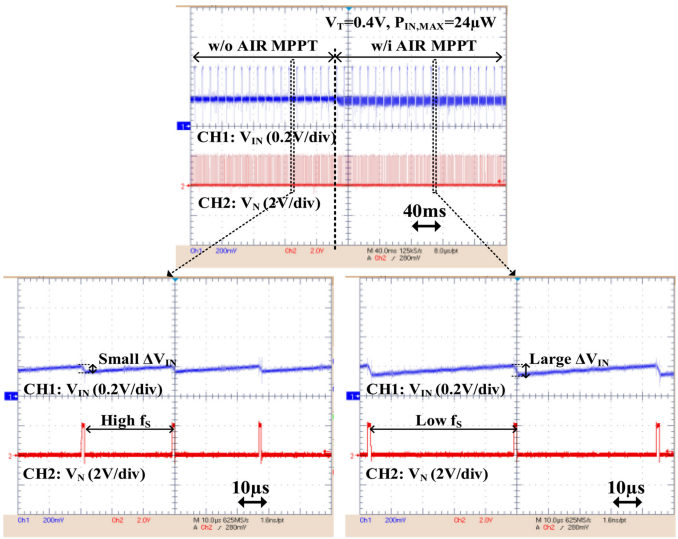

Fig. 21. Measured $V_{\rm IN}$ and V_N of the proposed energy harvesting system with and without the AIR MPPT control.

Fig. 20 shows the measured waveforms of the proposed energy harvesting system when V_T abruptly changes. The voltage source V_T with series resistor R_T (1.68 kΩ) is used to emulate the TEGs. V_T varies from 0.3 to 0.5 V and from 0.5 to 0.3 V to verify the MPPT operation of the system. A potentiometer is used as an emulated load. Initially, $V_{\rm IN}$ is regulated at 0.15 V, which is MPP of TEG with 0.3 V V_T. When V_T increases to 0.5 V, V_T is monitored at the following $V_{\rm OC}$ sensing phase. $V_{\rm IN}$ is regulated at 0.25 V, which is MPP, and $V_{\rm OUT}$ increases due to increased input power. When V_T decreases to 0.3 V, 0.3 V V_T is sensed, and $V_{\rm IN}$ is regulated at MPP, 0.15 V in this case. Because input power gets smaller, $V_{\rm OUT}$ decreases.

Fig. 21 shows the measured waveforms of the system when the proposed AIR MPPT control is turned ON and OFF. The external switches mentioned previously are used to control the delay levels of the STC. Without the AIR MPPT control, smaller $\Delta V_{\rm IN}$ is achieved due to higher f_S. After applying the AIR MPPT control, f_S is reduced and $\Delta V_{\rm IN}$ gets larger to increase η_{E-E}.

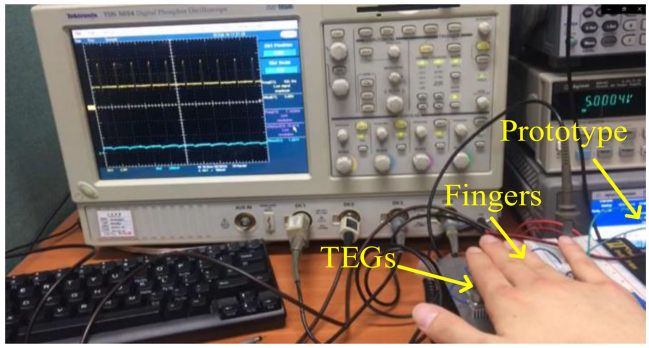

Fig. 22. Test environment of the proposed energy harvesting system with real TEG.

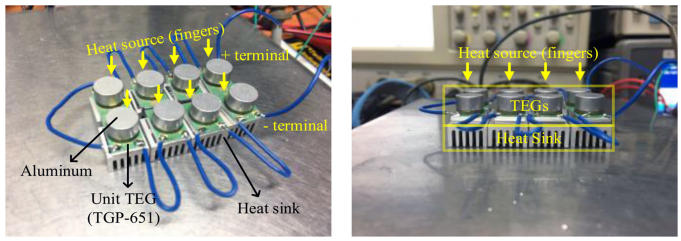

Fig. 23. TEGs to verify the proposed system with heat energy from human body.

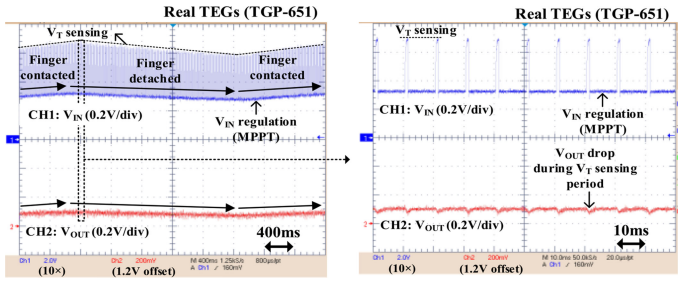

Fig. 24. Measured waveforms of the proposed energy harvesting system with real TEGs applied with human heat energy.

Fig. 22 shows the test environment to verify feasibility of the proposed system with real TEGs and heat energy from the human body. The TEGs are contacted with human fingers to apply ΔT. Fig. 23 shows the real TEGs used in this measurement. Eight series-connected TEGs [33] with a heat sink that maintains ΔT are made to generate reasonable voltage and power with human heat energy. The heat energy is delivered to TEG with aluminum. Fig. 24 shows the measured waveforms of the proposed system with real TEGs applied with human heat energy. Before the TEGs enter the thermal equilibrium state, ΔT goes up to 1.4 °C with human fingers. A 1.2 V offset is applied to channel 2 of the oscilloscope to emphasize $V_{\rm OUT}$ behaviors. When the TEGs are contacted with the fingers, V_T increases because ΔT increases. If the fingers are detached from the TEGs, ΔT decreases. Therefore, V_T also decreases. Even with this V_T variations, the proposed system keeps monitoring the changing V_T and tracking MPP. At the V_T sensing phase, no energy can be harvested from the TEGs. Therefore, $V_{\rm OUT}$ decreases.

TABLE I
COMPARISON OF THE THERMOELECTRIC ENERGY HARVESTING SYSTEM WITH STATE-OF-THE-ART SYSTEMS

	[14]	[18]	[24]	[5]	[22]	[23]	[25]	[26]	This work
Process	180-nm CMOS	350-nm CMOS	320-nm BCD	40-nm CMOS	130-nm CMOS	130-nm CMOS	65-nm CMOS	65-nm CMOS	180-nm CMOS
Minimum power	2 μW	153 μW	21 μW[6]	31 μW	80 μW	20 μW[3]	210 μW	20 μW	**6 μW**
Startup power	8 μW[1]	No startup	N.A.	59 μW	80 μW	2.42 mW [3],[4]	210 μW	2.2 mW	37 μW
Efficiency at low power ($P_{IN,MAX}$)*	45% η_{CHR} (24 μW)[1]	62% η_{CHR} (0.2mW)[7]	53% η_{E-E} (152μW)[7]	33% η_{E-E} (31 μW)[2]	33% η_{E-E} (80 μW)	22% η_{CHR} (24 μW)[3],[5]	47% η_{E-E} (210 μW)	53% η_{E-E} (24 μW)[2]	**63% η_{E-E} (24 μW)**
Peak efficiency ($P_{IN,MAX}$)	51% η_{CHR} (39 μW)	72% η_{CHR} (7.81 mW)	64% η_{E-E} (464 μW)	58% η_{E-E} (245 μW)	61% η_{E-E} (4.5 mW)	83% η_{CHR} (4.5 mW)[3]	71% η_{E-E} (2 mW)	71.5% η_{E-E} (320 μW)	**82% η_{E-E} (214 μW)**
Self-startup	Electrical	X	Other high -voltage sources (PV, piezo)	Mechanical	Transformer	Electrical+ RF kick-start	Electrical	Electrical	Electrical
MPPT	X	O	O	O	O	O	O	O	O

[1]Estimated from the efficiency versus output power curve.
[2]Estimated from the output power versus V_T curve.
[3] $R_T = 5\ \Omega$ is assumed.
[4]Only electrical startup is considered.
[5]Estimated from the efficiency versus. input voltage curve.
[6]TEG only.
[7]No efficiency data are reported at the low-power region.
*Efficiencies at similar $P_{\mathrm{IN,MAX}}$ are reported for a fair comparison.
PV: Photovoltaic

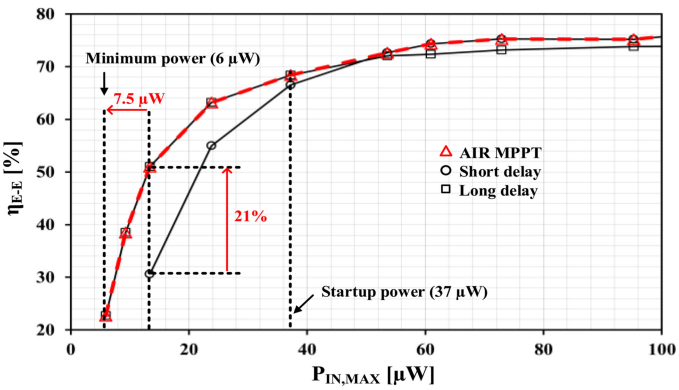

Fig. 25. Measured η_{E-E} of the proposed energy harvesting system in the low-power region (<100 μW).

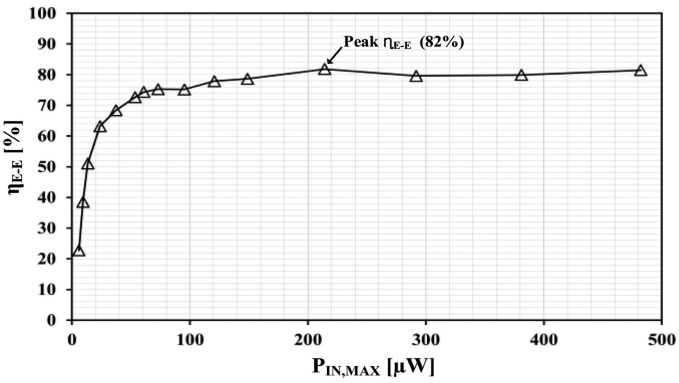

Fig. 26. Measured η_{E-E} of the proposed energy harvesting system for $P_{\mathrm{IN,MAX}}$ = 0–480 μW.

Fig. 25 shows the measured η_{E-E} of the proposed energy harvesting system in the low-power region (<100 μW). AIR MPPT adaptively controls the input ripple by selecting the delay levels and enhances η_{E-E} by 21% at $P_{\mathrm{IN,MAX}} = 13\ \mu$W. Moreover, the minimum $P_{\mathrm{IN,MAX}}$ is 6 μW, which is improved by 7.5 μW with AIR MPPT. η_{E-E} is 73% at $P_{\mathrm{IN,MAX}} = 54\ \mu$W. The startup power is 37 μW. Fig. 26 shows the measured η_{E-E} of the proposed system for $P_{\mathrm{IN,\ MAX}}$ = 0–480 μW. A peak η_{E-E} of 82% is achieved. Table I summarizes a comparison of our method with those presented in other studies. The self-startup scheme in the proposed system provides a minimum power of 6 μW. To compare the performance in the low-input power region, efficiencies at similar $P_{\mathrm{IN,\ MAX}}$ are reported. Because of the AIR MPPT technique, η_{E-E} in the low-power region is 63%. The peak efficiency of the proposed system is 82% at $P_{\mathrm{IN,\ MAX}}$ = 214 μW.

VI. CONCLUSION

A high-efficiency charger for low-power thermoelectric energy harvesting with the proposed AIR MPPT technique to improve the end-to-end efficiency is introduced in this paper. The AIR MPPT enhances the efficiency in the low-power region by taking into account not only the charger loss but also the extraction loss. It is analyzed and simulated that the end-to-end efficiency is highly dependent on the amplitude of the input ripple and switching frequency in the low-power region. On the basis of the analysis, the AIR MPPT technique controls the input ripple to enhance the end-to-end efficiency by controlling the switching frequency. The AIR MPPT technique is realized with an AIR MPPT controller consisting of an STC and LPD. Furthermore, the proposed charger enables fully electrical startup because of an LPS. A prototype of the proposed system is implemented using 180-nm CMOS technology. Improvements in the

end-to-end efficiency of 21% and minimum power of 7.5 μW are achieved with the AIR MPPT technique. The prototype provides 63% end-to-end efficiency in the low-power region (24 μW). The startup power and minimum power of the prototype are 37 and 6 μW, respectively. The maximum end-to-end efficiency is 82% at 214-μW input power.

REFERENCES

[1] Y. Zhang, L. Xu, Q. Dong, J. Wang, D. Blaauw, and D. Sylvester, "Recryptor: A reconfigurable cryptographic Cortex-M0 processor with in-memory and near-memory computing for IoT Security," *IEEE J. Solid-State Circuits*, vol. 53, no. 4, pp. 995–1004, Apr. 2018.

[2] S. Oh *et al.*, "A 2.5nJ duty-cycled bridge-to-digital converter integrated in a 13 mm^3 pressure-sensing system," in *Proc. IEEE Int. Solid-State Conf. Dig. Tech. Papers*, 2018, pp. 328–329.

[3] J. Jeong, S. Jeong, C. Kim, D. Sylvester, and D. Blaauw, "A 42nJ/conversion on-demand state-of-charge indicator for miniature IoT Li-ion batteries," in *Proc. VLSI Circuits Symp. Dig. Tech. Papers*, Jun. 2017, pp. 206–207.

[4] M. Cho *et al.*, "A 6 $\times$ 5 $\times$ 4 mm^3 general purpose audio sensor node with a 4.7 μW audio processing IC," in *Proc. VLSI Circuits Symp. Dig. Tech. Papers*, Jun. 2017, pp. 312–313.

[5] Y. K. Ramadass and A. P. Chandrakasan, "A battery-less thermoelectric energy harvesting interface circuit with 35 mV startup voltage," *IEEE J. Solid-State Circuits*, vol. 46, no. 1, pp. 333–341, Jan. 2011.

[6] M. Kishi *et al.*, "Micro thermoelectric modules and their application to wristwatches as an energy source," in *Proc. Int. Conf. Thermoelectrics*, 1999, pp. 301–307.

[7] S. Lineykin and S. Ben-Yaakov, "Modeling and analysis of thermoelectric modules," *IEEE Trans. Ind. Appl.*, vol. 43, no. 2, pp. 505–512, Mar./Apr. 2007.

[8] P. Spies, M. Pollak, and G. Rohmer, "Energy harvesting for mobile communication devices," in *Proc. 29th INTELEC*, Oct. 2007, pp. 481–488.

[9] I. Doms, P. Merken, C. Van Hoof, and R. P. Mertens, "Capacitive power management circuit for micropower thermoelectric generators with a 1.4 μA controller," *IEEE J. Solid-State Circuits*, vol. 44, no. 10, pp. 2824–2833, Oct. 2009.

[10] E. J. Carlson, K. Strunz, and B. P. Otis, "A 20 mV input boost converter with efficient digital control for thermoelectric energy harvesting," *IEEE J. Solid-State Circuits*, vol. 45, no. 4, pp. 741–750, Apr. 2010.

[11] P.-H. Chen and P.-Y. Fan, "An 83.4% peak efficiency single-inductor multiple-output based adaptive gate biasing DC-DC converter for thermoelectric energy harvesting," *IEEE Trans. Circuits Syst. I: Reg. Papers*, vol. 62, no. 2, pp. 405–412, Feb. 2015.

[12] M. Alhawari, B. Mohammad, H. Saleh, and M. Ismail, "An efficient zero current switching control for L-based DC-DC converters in TEG applications," *IEEE Trans. Circuits Syst. II: Express Briefs*, vol. 64, no. 3, pp. 294–298, Mar. 2017.

[13] P.-S. Weng, H.-Y. Tang, P.-C. Ku, and L.-H. Lu, "50 mV-input battery-less boost converter for thermal energy harvesting," *IEEE J. Solid-State Circuits*, vol. 48, no. 4, pp. 1031–1041, Apr. 2013.

[14] M. Dezyani, H. Ghafoorifard, S. Sheikhaei, and W. A. Serdijin, "A 60 mV input voltage, process tolerant start-up system for thermoelectric energy harvesting," *IEEE Trans. Circuits Syst. I: Reg. Papers*, vol. 65, no. 10, pp. 3568–3577, Oct. 2018.

[15] P.-H. Chen *et al.*, "0.18-V input charge pump with forward body biasing in startup circuit using 65 nm CMOS," in *Proc. IEEE Custom Integr. Circuits Conf.*, Sep. 2010, pp. 1–4.

[16] J. Goeppert and Y. Manoli, "Fully integrated start-up at 70 mV of boost converters for thermoelectric energy harvesting," *IEEE J. Solid-State Circuits*, vol. 51, no. 7, pp. 1716–1726, Jul. 2016.

[17] P.-H. Chen *et al.*, "An 80 mV startup dual-mode boost converter by charge-pumped pulse generator and threshold voltage tuned oscillator with hot carrier injection," *IEEE J. Solid-State Circuits*, vol. 47, no. 11, pp. 2554–2562, Nov. 2012.

[18] J. Kim and C. Kim, "A DC–DC boost converter with variation-tolerant MPPT technique and efficient ZCS circuit for thermoelectric energy harvesting applications," *IEEE Trans. Power Electron.*, vol. 28, no. 8, pp. 3827–3833, Aug. 2013.

[19] J. Katic, S. Rodriguez, and A. Rusu, "A dual-output thermoelectric energy harvesting interface with 86.6% peak efficiency at 30 μW and total control power of 160 nW," *IEEE J. Solid-State Circuits*, vol. 51, no. 8, pp. 1928–1937, Aug. 2016.

[20] J. Katic, S. Rodriguez, and A. Rusu, "A high-efficiency energy harvesting interface for implanted biofuel cell and thermal harvesters," *IEEE Trans. Power Electron.*, vol. 33, no. 5, pp. 4125–4134, May 2018.

[21] S. C. Bautista, A. Eladawy, A. N. Mohieldin, and E. S. Sinencio, "Boost converter with dynamic input impedance matching for energy harvesting with multi-array thermoelectric generators," *IEEE Trans. Ind. Electron.*, vol. 61, no. 2, pp. 5345–5353, Oct. 2014.

[22] J.-P. Im, S.-W. Wang, S.-T. Ryu, and G.-H. Cho, "A 40 mV transformer-reuse self-startup boost converter with MPPT control for thermoelectric energy harvesting," *IEEE J. Solid-State Circuits*, vol. 47, no. 12, pp. 3055–3067, Dec. 2012.

[23] A. Shrivastava, N. E. Roberts, O. U. Khan, D. D. Wentzloff, and B. H. Calhoun, "A 10 mV-input boost converter with inductor peak current control and zero detection for thermoelectric and solar energy harvesting with 220 mV cold-start and 14.5 dBm, 915 MHz RF kick-start," *IEEE J. Solid-State Circuits*, vol. 50, no. 8, pp. 1820–1832, May 2015.

[24] M. Dini, A. Romani, M. Filippi, V. Bottarel, G. Ricotti, and M. Tartagni, "A nanocurrent power management IC for multiple heterogeneous energy harvesting sources," *IEEE Trans. Power Electron.*, vol. 30, no. 10, pp. 5665–5680, Oct. 2015.

[25] D. Rozgic and D. Markovic, "A miniaturized 0.78-mW/cm^2 autonomous thermoelectric energy-harvesting platform for biomedical sensors," *IEEE Trans. Biomed. Circuits Syst.*, vol. 11, no. 4, pp. 773–783, Aug. 2017.

[26] Z. Luo, L. Zeng, B. Lau, Y. Lian, and C.-H. Heng, "A sub-10 mV power converter with fully integrated self-start, MPPT, and ZCS control for thermoelectric energy harvesting," *IEEE Trans. Circuits Syst. I: Reg. Papers*, vol. 65, no. 5, pp. 1744–1757, May 2018.

[27] A. Mirocha and P. Dziurdzia, "Improved electrothermal model of the thermoelectric generator implemented in SPICE," in *Proc. Int. Conf. Signals Electron. Syst.*, Sep. 2008, pp. 317–320.

[28] Micropelt, MPG-D751 Micropelt Thermogenerator Datasheet, Germany, 2013. [Online]. Available: http://www.micropelt.com

[29] Tellurex, Tellurex Thermoelectric Energy Harvester—G1-1.0-127-1.27. 2007. [Online]. Available: http://www.tellurex.com

[30] Y. K. Ramadass, "Energy processing circuits for low-power applications," Ph.D. dissertation, Dept. Elect. Eng. Comput. Sci., Massachusetts Inst. Technol., Cambridge, MA, Jun. 2009.

[31] F.-F. Ma, W.-Z. Chen, and J.-C. Wu, "A monolithic current-mode buck converter with advanced control and protection circuits," *IEEE Trans. Power Electron.*, vol. 22, no. 5, pp. 1836–1846, Sep. 2007.

[32] J. A. A. Qahouq, "Control scheme for sensorless operation and detection of CCM and DCM operation modes in synchronous switching power converters," *IEEE Trans. Power Electron.*, vol. 25, no. 10, pp. 2489–2495, Oct. 2010.

[33] Micropelt, TGP-651 Micropelt Thermogenerator Datasheet, Germany, 2014. [Online]. Available: http://www.micropelt.com

Junwon Jeong (S'12) received the B.S. and Ph.D. degrees in electrical engineering from Korea University, Seoul, South Korea, in 2012 and 2019, respectively.

He spent a research internship as a Visiting Scholar with the University of Michigan, Ann Arbor, MI, in 2015 for ultralow power battery state-of-charge indicator design. He joined Samsung Electronics in 2019 as a Staff Engineer. His research interests include integrated power management system designs, low-voltage low-power complementary metal oxide–semiconductor analog circuit designs, energy harvesting circuit designs, and fuel gauging circuit designs.

Minseob Shim (S'13–M'18) received the B.S. and Ph.D. degrees in electrical engineering from Korea University, Seoul, South Korea, in 2012 and 2018, respectively.

He spent a research internship as a Visiting Scholar with the University of Michigan in Ann Arbor, MI, in 2015 for SAR ADC with the energy-efficient comparator design. He joined Korea Electrotechnology Research Institute in 2018 as a Senior Researcher. His research interests include integrated power management system, low-voltage analog and mixed-signal integrated circuit, and analog-to-digital converter designs.

Junyoung Maeng (S'14) received the B.S. degree in electrical engineering from Hongik University, Seoul, South Korea, in 2014. He is currently working toward the integrated M.S. and Ph.D. degrees in electrical engineering from Korea University, Seoul, South Korea.

In 2016, he was a Visiting Researcher with the University of Texas at Dallas, TX, USA. His research interests include integrated power management system designs, low-power complementary metal oxide–semiconductor analog circuit designs, energy-harvesting circuit designs, and dc–dc converters.

Mr. Maeng was the recipient of the 2017–2018 IEEE International Circuit Design Contest sponsored by the Solid-State Circuits Society.

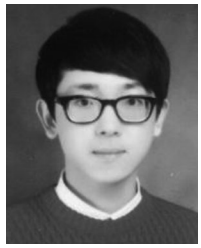

Inho Park (S'16) received the B.S. degree in electrical engineering, in 2016, from Korea University, Seoul, South Korea, where he is currently working toward the integrated M.S. and Ph.D. degrees.

His research interests include integrated power management system designs, high-voltage silicon-based power converter designs, low-power complementary metal oxide–semiconductor analog circuit designs, and energy-harvesting circuit designs.

Chulwoo Kim (S'98–M'02–SM'06) received the B.S. and M.S. degrees in electronics engineering from Korea University, Seoul, South Korea, in 1994 and 1996, respectively, and the Ph.D. degree in electrical and computer engineering from the University of Illinois at Urbana–Champaign, IL, USA, in 2001.

In 1999, he was a Summer Intern with the Design Technology, Intel Corporation, Santa Clara, CA, USA. In 2001, he joined the IBM Microelectronics Division, Austin, TX, USA, where he was involved in cell processor design. Since 2002, he has been with the School of Electrical Engineering, Korea University, where he is currently a Professor. He was a Visiting Professor with the University of California at Los Angeles in 2008 and the University of California, Santa Cruz, CA, USA in 2012. He has coauthored two books, namely, complementary metal oxide–semiconductor *Digital Integrated Circuits: Analysis and Design* (McGraw Hill, 2014, fourth edition) and *High-Bandwidth Memory Interface* (Springer, 2013). His current research interests include the areas of wireline transceivers, memory, power management, and data converters.

Dr. Kim was the recipient of the Samsung HumanTech Thesis Contest Bronze Award in 1996, ISLPED Low-Power Design Contest Award in 2001 and 2014, DAC Student Design Contest Award in 2002, SRC Inventor Recognition Awards in 2002, Young Scientist Award from the Ministry of Science and Technology, South Korea, in 2003, Seoktop Award for excellence in teaching in 2006 and 2011, ASP-DAC Best Design Award in 2008, Special Feature Award in 2014, and Korea Semiconductor Design Contest: Ministry of Trade, Industry and Energy Award in 2013. He was selected as a Distinguished Lecturer of the IEEE Solid-State Circuits Society from 2015 to 2016. He served on the Technical Program Committee of the IEEE International Solid-State Circuits Conference and as a Guest Editor for the IEEE JOURNAL OF SOLID-STATE CIRCUITS. He is currently on the Editorial Board of the IEEE TRANSACTIONS ON VLSI SYSTEMS.